Koukouvinis, P., Gavaises, M., Li, J. & Wang, L. (2016). Large Eddy Simulation of Diesel injector including cavitation effects and correlation to erosion damage. Fuel, 175, pp. 26-39. doi: 10.1016/j.fuel.2016.02.037

Large Eddy Simulation of Diesel Injector including cavitation effects and correlation to erosion damage

Phoevos Koukouvinis[*,a], Manolis Gavaises[a], Jason Li[b], Lifeng Wang[b]

[a] City University London, Northampton Square EC1V 0HB, United Kingdom

[b] Caterpillar Inc, Mossville, IL 61552 US

[*]Corresponding author, tel: +44(0)7561883907, email: foivos.koukouvinis.1@city.ac.uk

Large Eddy Simulation of Diesel Injector including cavitation effects and correlation to erosion damage

Phoevos Koukouvinis[*,a], Manolis Gavaises[a], Jason Li[b], Lifeng Wang[b]

[a] City University London, Northampton Square EC1V 0HB, United Kingdom

[b] Caterpillar Inc, Mossville, IL 61552 US

[*]Corresponding author: foivos.koukouvinis.1@city.ac.uk

Abstract. The present paper focuses on erosion development due to cavitation inside Diesel injectors. Two similar injector designs are discussed both in terms of numerical simulation and experimental results from X-ray CT scans. In order to capture the complex flow field and cavitation structures forming in the injector, Large Eddy Simulation along with a two phase homogenous mixture model were employed and compressibility of the liquid was included as well. During the simulation, pressure peaks have been found in areas of vapour collapse, with magnitude beyond 4000bar, which is higher than the yield stress of common materials employed in the manufacturing of such injectors. The locations of such pressure peaks correspond well with the actual erosion locations as found from X-ray scans. The present work's novelty is to correlate pressure peaks due to vapour collapse with erosion development in industrial injectors with moving needle including comparison with experiments.

Keywords: Diesel injector, LES, Cavitation, Erosion, X-Ray CT scans.

1. Introduction

Diesel injection systems play a fundamental role in internal combustion engines since they affect the formation of the fuel spray, atomization and combustion, the formed emissions and the engine efficiency. The jet velocities formed are of the order of 500m/s, with upstream pressures around 2000bar. Current trends show injection pressures to even rise to 3000bar, in order to meet the future EU legislations in emissions. However, higher pressure levels causes very high velocities through the tight passages in the Diesel injector and strong accelerations in sharp direction changes (corners, fillets etc.), which lead to static pressure dropping locally below the saturation pressure and causing cavitation. Furthermore, cavitation may lead to erosion damage and serious degradation of the injector performance, even catastrophic injector failure, which could damage the engine, if the injector tip breaks off.

Various researchers have worked on the subject of cavitation development inside Diesel injectors under varying assumptions; Sezal et al. worked on simple 2D axis-symmetric nozzles [1] and 3D nozzles [1, 2] with a fully compressible approach, capable of predicting cavitation collapse pressure peaks that could be linked to cavitation erosion. Salvador et al. have done extensive work on Diesel injector cavitation, starting from validation studies [3], examining various geometrical features [4] and needle lift influence [5] on the flow pattern inside the injector. In continuation of the aforementioned work, Molina et al. [6] examined the influence of elliptical orifices on cavitation formation and Salvador et al. [7] performed LES studies in Diesel injector nozzles using OpenFOAM. However all the aforementioned literature work did not involve needle motion; instead needle was fixed either at full or partial lift. A recent numerical work by Örley et al. [8] on Diesel injectors involves the immersed boundary method, needle motion, compressibility of liquid, vapour and free gas, though the focus is mainly on the developed turbulent structures and less on pressure peak/erosion development.

On the other hand, several works have included the needle motion for the prediction of flow pattern inside the injector, however either resorted to using RANS or omitted compressibility effects. For example Patouna [9] focused on the simulation of injectors at steady or moving needle conditions, however the liquid was assumed incompressible and there was no effort to correlate with possible erosion development. Strotos et al. [10] studied the thermodynamic effects of Diesel fuel heating/cooling inside the Diesel injectors at both steady and moving needle conditions, with main interest on next-generation injectors that could reach up to discharge pressures of 3000bar. Devassy et al. [11] implemented a 1D-3D coupling for Diesel injector simulations throughout the whole injection pulse; the 3D simulation involved needle motion and a simplistic liquid compressibility model.

There have been several efforts for the prediction of the cavitation erosion in Diesel injectors, see e.g. the work of Gavaises et al. [12] and Koukouvinis et al. [13]. The aim of the current work is to simulate the flow inside a Diesel injector in a more fundamental level, including needle motion, compressibility effects of the liquid phase and also using a Large Eddy Simulation for describing turbulence. Mesh motion is necessary for describing the transient effects in the injector. The reason for employing compressibility effects is that the fuel density can vary as much as 10% within the injector [14], not to mention the high liquid velocities that can reach a Mach number of 0.5 or more. Furthermore, resorting to Large Eddy Simulation techniques is because RANS/URANS are inadequate for capturing the complicate vortex patterns which affect cavitation formation [15], while even modified RANS turbulence models are situational [16]. To the authors knowledge there is no other work in literature that resolves the compressible turbulent flow in a moving needle Diesel injector with LES, including the prediction of vapour collapse pressures and correlation with actual erosion damage from CT scans of actual injectors. Furthermore, the methodology discussed in the present paper involves a modified cavitation model, in order to move closer towards thermodynamic equilibrium; if such a modification is not employed then unphysically high tension is predicted in the liquid.

The current paper is organized as follows: first an indicative description of two injector tip geometries will be given, along with testing conditions and X-ray scans of the erosion damage from the endurance test. Then, the numerical methodology will be presented. The simulation results of the Rayleigh collapse of a vaporous bubble is examined as a fundamental test case of the methodology used. Indeed, the aim of the current study is to detect the regions of the collapse of cavitation structures, which is directly linked with the formation of extreme local pressure and therefore erosion damage. Furthermore the simulation results of a simple throttle flow that has been previously studied by Edelbauer et al. [16] will be presented as a more applied benchmark case. Finally, indicative results of the simulated injectors will be shown and will be compared with the X-ray scans from the experiments, showing a good correlation.

2. Description of the examined injectors and testing conditions

2.1. Injector geometry and operating conditions

The examined injectors are common rail injectors. The accelerated cavitation test is performed in an endurance test rig, located at Caterpillar US research and development centre. Endurance testing is conducted for several thousand hours, with injection pressure at 1.1-1.5 times the injector rated operating pressure. The testing fuel is periodically replaced to maintain quality. The injectors are mounted on the head block of the test rig and the injected fuel is collected by the collector block and the rate tube, with downstream pressure adjusted by the pressure regulator at the end of the rate tube. The test rig also has a heat exchanger to keep Diesel fuel temperature controlled at around 40^{o}C in the fuel tank and a computer which collects data and controls the injection frequency.

Two injector designs are examined, which will be referred to as Design A and Design B hereafter. Both injectors have 5 hole tip and share exactly the same needle, as shown in Figure 1. Design A has cylindrical holes (k-factor 0), while Design B injector has slightly tapered holes (k-factor is 1.1). Moreover, Design B has a significantly smaller sac volume comparing to Design A. This characteristic makes the Design B tip somewhat shorter than the equivalent of Design A. A summary of the most important dimensions of the two injectors is given in Table I.

Table I. Important geometric dimensions of the examined injectors.

Geometric characteristics		Design A	Design B
Needle radius (mm)		1.711	1.711
Orifice length (mm)		1.261	1.262
Orifice diameter (mm)	Entrance - D_{in}	0.37	0.37
	Exit - D_{out}	0.37	0.359
Sac volume (mm^3)		3.35	1.19
$k-factor = (D_{in} - D_{out})/10$, D in μm		0	1.1

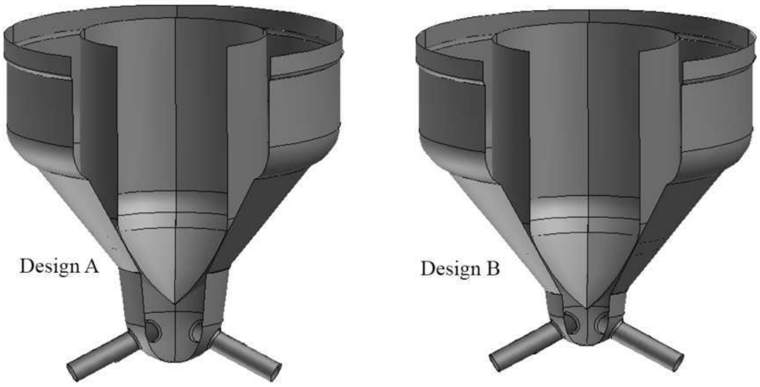

Figure 1. Comparative view of the two designs: Left is Design A and right Design B.

The injector operating pressure is ~1800bar with inlet fuel temperature at ~75^{o}C. The collector back pressure is ~50bar. Design B injector has a slightly higher needle lift, but shorter injection pulse duration comparing to Design A. The total injection duration is ~3ms. Figure 2 shows the pressure inlet boundary condition and needle motion for the two designs, as predicted using the 1-D system performance analysis software, developed internally by Caterpillar Inc. The 1-D model includes the entire hydraulic circuit of the endurance bench fuel systems as well as the electronic control system. The input parameters of the 1-D model include engine speed, fuel pressure and temperature, injection duration, and regulator back pressure, etc. In the present work, simulation results mainly of the opening phase of the injectors will be presented, i.e. for a lift from 0 to ~300μm (for Design A) or ~350μm (for Design B).

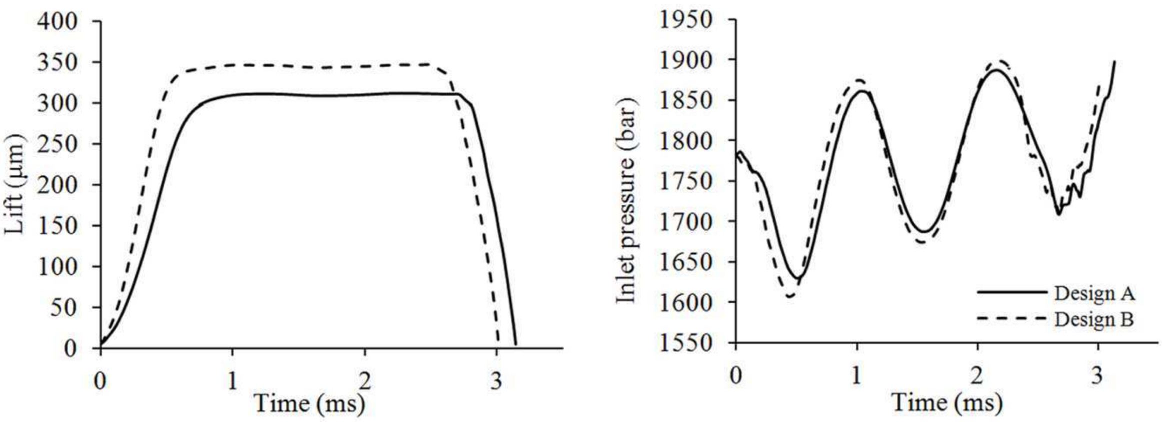

Figure 2. Needle motion and transient pressure inlet boundary condition for the two designs.

From hereafter the following naming convention will be used to refer to various injector parts, surfaces and volumes, see also Figure 3:

- The injector tip volume is split into several sub-volumes, which can be identified as follows, starting upstream the injector tip and following the fuel flow: *annulus*, *needle/needle seat passage*, *sac volume* and *orifice* or *hole*.

- The injector tip surfaces are split into the following: the surface of the *annulus* that corresponds to the larger diameter will be referred as *body*. The *needle seat* and the *needle* walls define the *passage* volume. *Sac wall* is bounding the *sac volume*. *Orifice entrance* is the geometrical transition (which is usually a fillet) from the *sac wall* to the *orifice* surfaces. The orifice surface may be split further into the *upper* and *lower surfaces*; here *upper surface* corresponds to the surface that is closer to the inlet, i.e. faces towards the upstream direction, and *lower surface* faces towards the downstream flow direction, i.e. the combustion/injection chamber.

For more information on injector operation, components and assembly the interested reader is addressed to [17].

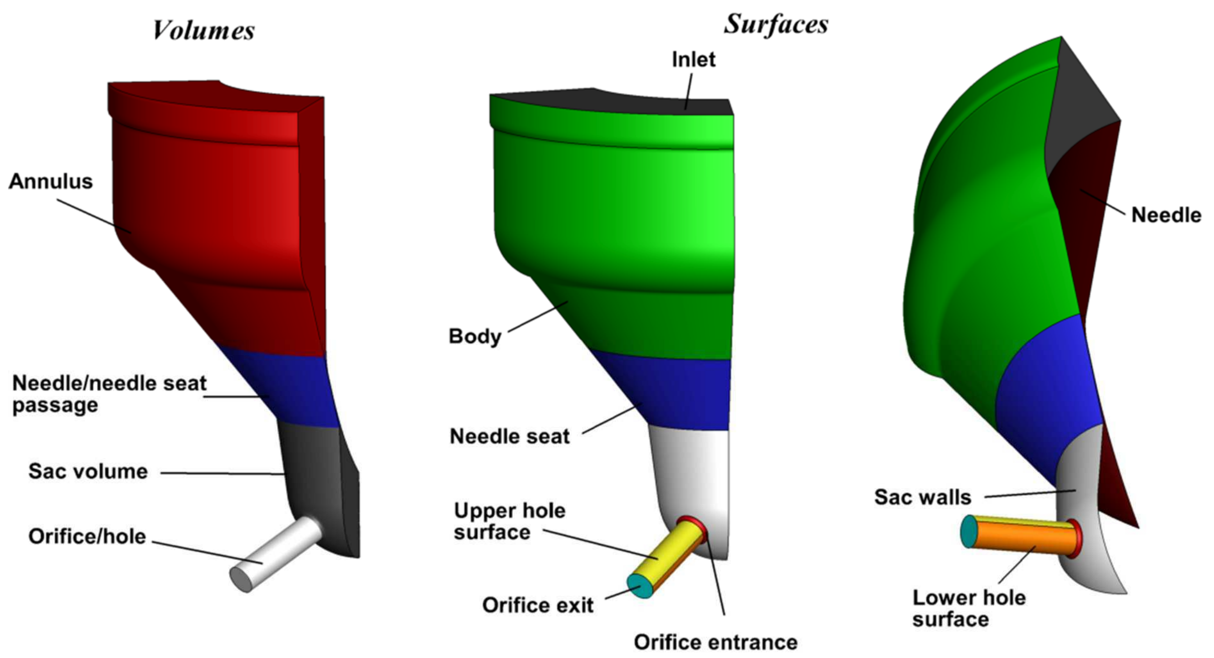

Figure 3. Naming convention of various injector sub-volumes (left) and surfaces (middle and right) to be used hereafter.

2.2. Injector endurance tests and X-ray erosion patterns

Figure 4 and Figure 5 show the X-ray CT scans of the sac/orifice and needles of four injectors with the same endurance test hours. Figure 4 shows the erosion patterns in two design A injectors, while Figure 5 shows the erosion patterns in two design B injectors. As can be seen from the relevant X-ray scans, both designs are susceptible to cavitation erosion damage. Design A injector has signs of erosion damage inside the sac volume that become apparent rather early, in the order of one thousand hours of continuous operation. Design B injector is less prone to erosion damage, since noticeable damage occurs significantly later, in the order of several thousand hours of continuous operation; even then the damage is minor, in the form of a slight pit near the orifice entrance. Regarding the damage in the nozzle holes, Design B injector is generally less prone to erosion damage, while the cylindrical hole of Design A has signs of damage at thousand hours, which progresses more aggressively with time comparing to Design B. The trend seems to change when considering the needle damage, since Design A needle is almost erosion free; there are only some minor, nearly negligible, signs of erosion, that do not show any change over time. Design B injector needle is more affected by erosion, since a deep indentation is visible in the form of a ring of radius ~0.6mm see Figure 5; however the erosion damage does not seem to progress after formation.

The experimental results obtained from the endurance tests suggest that the erosion patterns are consistent for Design B injector, that is a similar erosion trend develops for injectors tested, after similar time intervals. However this is not the case for Design A; even though erosion locations are in general the same, there is discrepancy in the erosion development among the same design after the same time interval. E.g. in Figure 4 the one sac volume seems to be much less affected by erosion damage than the other and on the other hand in one case the injector holes are practically ruined by erosion damage, while the other is barely affected by erosion damage. It is speculated that this effect is related to possible eccentric motion of the injector needle, that could alter the flow pattern inside the injector and consequently cavitation formation, and slight variations of the exact test conditions.

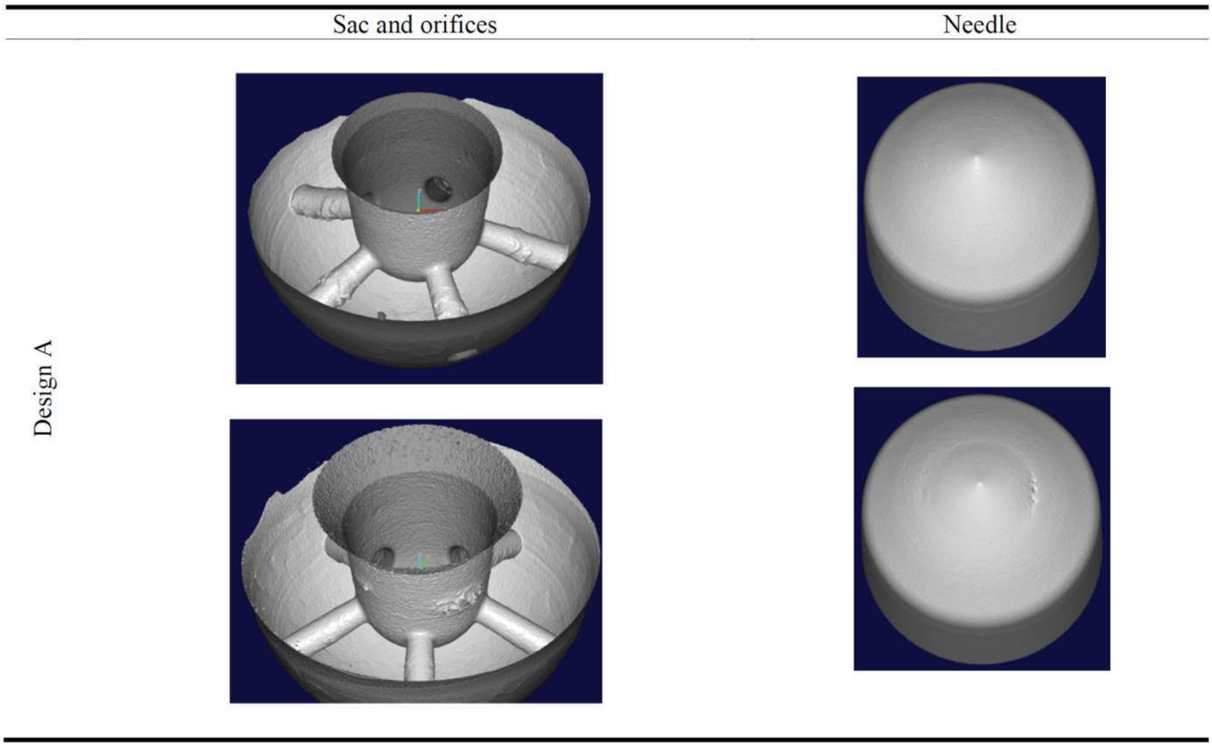

Figure 4. Erosion details at various locations for Design A, as found on the surfaces of two examined injectors after the same operation hours.

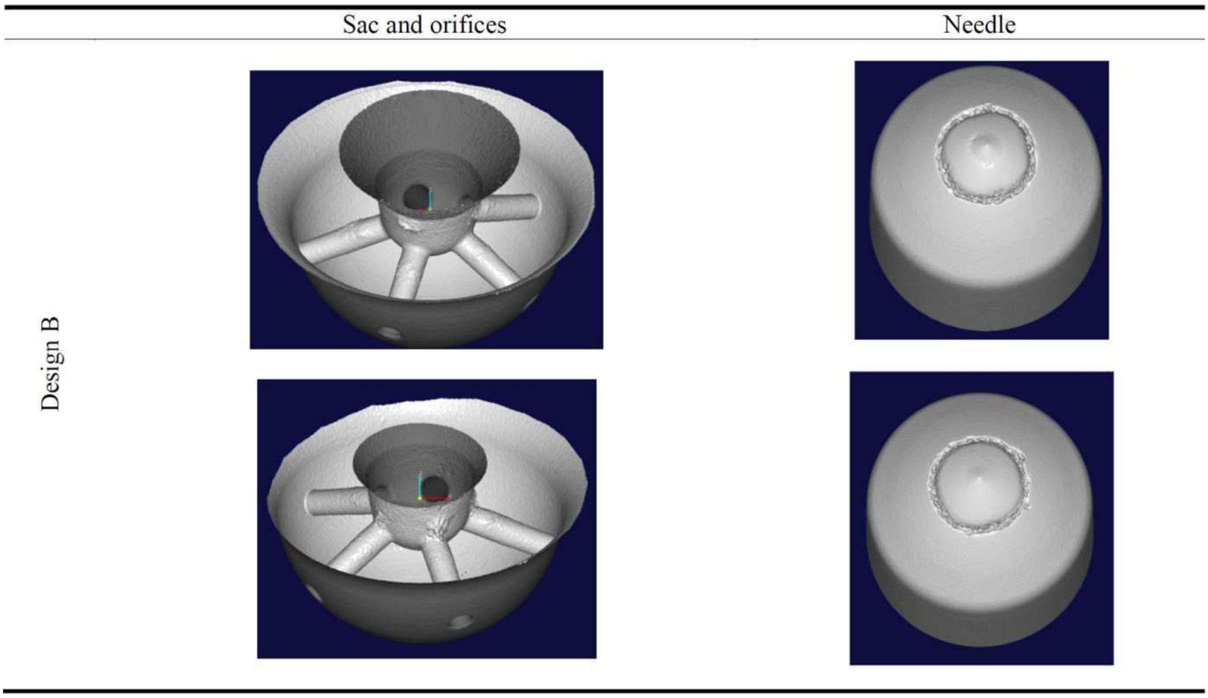

Figure 5. Erosion details at various locations for Design B, as found on the surfaces of two examined injectors after the same operation hours.

3. Numerical background

Numerical simulations presented in this work are based on a the solution of the Navier Stokes equations, using a commercial pressure-based solver, Fluent [18]. The equations solved consist of the continuity and momentum equations, while the energy equation has been omitted. The reason for omitting heat effects was the limited applicability of the Diesel properties library currently available [14]. As will be shown later, local pressures may reach or exceed 9000bar and, due to the polynomial nature of the Kolev properties library, negative densities may be predicted, which are meaningless; alternative libraries will be considered in future work as e.g. NIST Refprop [19], but applicability in such extreme cases is generally not guaranteed. In any case, since Diesel properties vary significantly with the pressure levels in the injection systems, both liquid phase viscosity and density are assumed variable, as functions of pressure only. For density, the Tait equation of state was used:

$$p = B\left[\left(\frac{\rho}{\rho_{sat,L}}\right)^{n} - 1\right] + p_{sat} \tag{1}$$

where $\rho_{sat,L}$ is the density at saturation pressure p_{sat}. This equation of state has the advantage that can handle both large and negative (up to a point) pressures. The values used for the simulations are summarized in the following table, including the liquid viscosity μ_L:

Table II. Liquid phase properties.

Property	Rayleigh collapse	Throttle case	Design A/Design B Injectors (properties estimated at 395K)
$\rho_{sat,L}$ (kg/m^3)	998.2	830	747.65
p_{sat} (Pa)	2340	4500	$1.1 \cdot 10^5$
B (MPa)	300	167	110
μ_L (Pa.s)	10^{-3}	$2.1 \cdot 10^{-3}$	$\log_{10}\left(10^6 \mu_L / \rho\right) = 0.035065275 - 0.000234373\ p/10^5$

For all materials the exponent n is set to 7.15, since such values correspond to weakly compressible materials such as liquids [20]. Properties for the injector flow are considered on an average temperature level of 395K. This value was estimated through simplified 1D analysis for the pressure levels in the injector [10], given a range of the discharge coefficient from ~0 (valve closed, estimated outlet temperature ~427K) to ~0.8 (valve fully open, estimated outlet temperature ~359K) and is an estimated average during the injection event; note that the theoretical minimum outlet temperature for the injectors is ~324K, for operation at a discharge coefficient of unity, which would apply for the ideal case without friction losses. Also, liquid dynamic viscosity is prescribed with a relation provided by N. Kolev [14], applied for the same temperature level as above.

For inclusion of cavitation effects, an additional transport equation is solved for tracking the vapour phase, of the form:

$$\frac{\partial(a\rho_v)}{\partial t} + \nabla(a\rho_v\mathbf{u}) = R_e - R_c \tag{2}$$

where a is the vapour fraction, ρ_v is the vapour density, $\mathbf{u}$ is the velocity field and R_e, R_c are the mass transfer rates for condensation (c) and evaporation (e), prescribed by the Zwart-Gerber-Belamri model [21]. Vapour properties are set considering the saturation conditions of each material:

Table III. Vapour phase properties.

Property	Rayleigh collapse	Throttle case	Injectors
ρ_V (kg/m^3)	0.0171	0.286	6.5
μ_V (Pa.s)	$9.75 \cdot 10^{-6}$	$7.5 \cdot 10^{-6}$	$7.5 \cdot 10^{-6}$

Here it must be mentioned that while vapour is treated as incompressible, the vapour/liquid mixture is compressible, due to mass transfer terms; in fact it can be proved that the dominant term affecting the mixture compressibility is the mass transfer term, see [22]. Moreover, under the assumption of cavitation formation at approximately constant pressure equal to saturation, the vapour density should be approximately constant. Of course, possible compressibility effects, such as shock waves, in the pure vapour phase cannot be captured in this way, but their effect on the results is questionable.

The two phase model is a homogenous mixture model that assumes mechanical equilibrium between the two phases, i.e. both liquid and vapour phase share the same pressure and velocity fields. The mass transfer model behaves as a non-thermodynamic equilibrium model, since metastable conditions of liquid tension, i.e. negative pressures, may develop. While such scenarios have been found in delicate laboratory experiments, see for example [22-25], it is rather questionable if they are possible to exist in industrial flows and especially the highly violent flow inside a throttle or a diesel injector. For this reason, the mass transfer terms have been increased in order to limit the existence of negative pressures inside the computational domain as much as possible; after the tuning the minimum pressure inside the throttle is approximately -1bar and in the injector is approximately -20bar. Without tuning the liquid tension would be at least one order of magnitude higher.

Apart from the simple benchmark case of the Rayleigh collapse, LES methodologies were used for the rest cases, in order to capture the complicated turbulent structures which significantly contribute to the cavitation structures. The throttle case was simulated with the Coherent Structure Model (CSM) [16, 26] in order to be consistent with the relevant published results [16], whereas the injectors were simulated with the Wall Adapted Local Eddy-viscosity (WALE) LES model [27]. Both models are much better behaved in wall-bounded flows, since the eddy viscosity diminishes at the near wall locations, contrary to the standard Smagorinsky model.

4. Simulations

4.1. Collapse of a spherical vapour bubble

Since the aim of the two phase model employed is to predict the Rayleigh collapse of a vaporous structures in the liquid fuel, it is reasonable to test the capability of the model in the prediction of collapse of a spherical vapour bubble in an infinite liquid domain of higher pressure. For this test, a simple 2D-axis symmetric configuration is used involving water at pressure of 1bar and a vapour bubble of R_0=10μm at saturation conditions, i.e. 2339Pa. It is important to mention that the farfield boundary is set at 100 bubble radii away from the bubble; early trials have shown that setting the boundary closer leads to an earlier collapse, due to bias imposed from the boundary. The configuration resembles the well known Rayleigh collapse, where the radius of the bubble reduces in an accelerating manner, with bubble wall velocity tending to infinity. In that case, the bubble collapse velocity is given by the following relation [22]:

$$\frac{dR}{dt} = -\sqrt{\frac{2}{3}\frac{p_\infty - p_v}{\rho}\left[\left(\frac{R_0}{R}\right)^3 - 1\right]} \quad (6)$$

which can be integrated numerically, till the characteristic Rayleigh time τ of bubble collapse:

$$\tau \cong 0.915 R_0 \sqrt{\frac{\rho}{p_\infty - p_v}} \quad (7)$$

For the aforementioned conditions, the Rayleigh time is τ= 0.925μs. In Figure 6 comparison between the theoretical solution and the numerical solution with the two phase model is provided, showing an excellent agreement. This gives confidence that the results of the two phase model can be applied in arbitrary shaped cavitation structures, for which there is no theoretical solution; such structures however develop inside the injector and it is crucial that their collapse is captured properly.

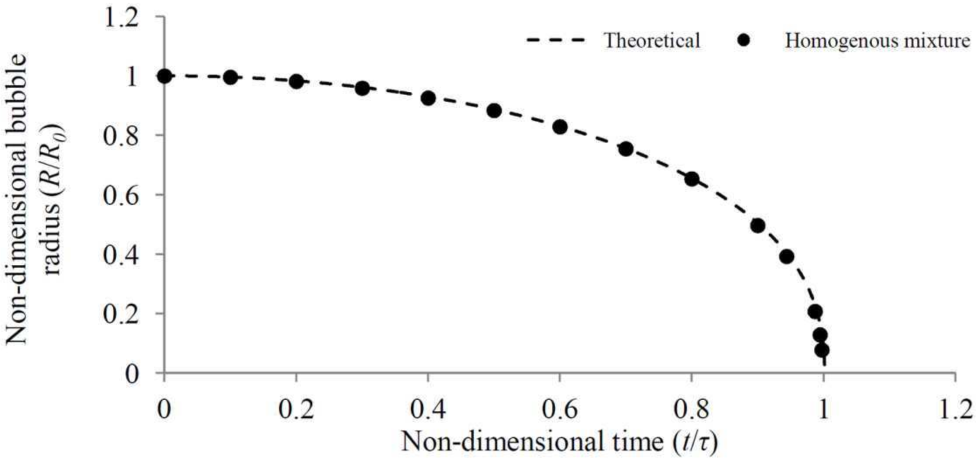

Figure 6. Rayleigh collapse of a vapour bubble with the two phase model employed.

4.2. Throttle case

The throttle case examined is described in great detail in [16]; the throttle is formed on a metal plate sandwiched between two sapphire glasses for external observations. The cross-section of the throttle is 295x300μm and has a length of 993μm. A total pressure inlet is imposed 13 throttle widths upstream and a constant pressure outlet is imposed 30 throttle widths downstream, in order to minimize boundary influence as much as possible. The case examined has a pressure difference

300bar to 120bar from inlet to outlet and velocities up to ~250m/s develop inside the constriction. From experimental observations, significant cavity shedding occurs, with cavitation reaching almost till the middle of the channel length [16] and erosion is estimated to start from 120μm till 730μm from the channel entrance, while being heavily pronounced in the area between 260-530μm from the channel entrance [16].

Given the flow conditions inside the throttle, the Reynolds number is ~29000, which corresponds to a Taylor length scale, λ_g [28]:

$$\lambda_g = \sqrt{10}\,\mathrm{Re}^{-0.5}\,L = 5.5\mu m \tag{10}$$

where L is an indicative length scale of the geometry; here the throttle width has been used, i.e. 300μm. The Taylor length scale is useful for LES studies, since it can be used to estimate the transition between inertial to viscous scales. The goal of the LES study is to simulate the anisotropic scales larger than the Taylor length scale and to model the smaller viscous isotropic scales. Given this, the resolution in the core of the throttle is 5μm, with refinement near the walls. The topology of the mesh is block structured, with refinement at the throttle region. The time step used is 4ns, which corresponds to a CFL of ~0.2, enabling to capture the highly transient fluid patterns. The simulation was run for 50μs; assuming a Strouhal number of 0.3, commonly found in cavity shedding [22], the period of one cavity oscillation is ~4μs, thus the total simulation time is more than 12 oscillation periods which was considered enough for collecting statistics of the flow field.

In Figure 7 indicative results from the simulation are shown; the throttle is placed in such a way that its plane of symmetry is positioned on the *xy* plane, i.e. the throttle is formed as an extruded surface of the shown geometry in the normal direction. Both plots focus in the area of interest, at the throttle. The flow moves from the negative to the positive direction of the x-axis.

As shown in Figure 7a, the averaged cavity length spans from the throttle entrance till a length of 0.5mm downstream the throttle, in accordance with the data reported in the work of Edelbauer et al. [16]. In Figure 7b indicative locations of accumulated pressure peaks over the simulation time of magnitude over 500bar are shown; these peaks are caused by the collapse of cavitation structures and may reach values of even 1600bar locally.

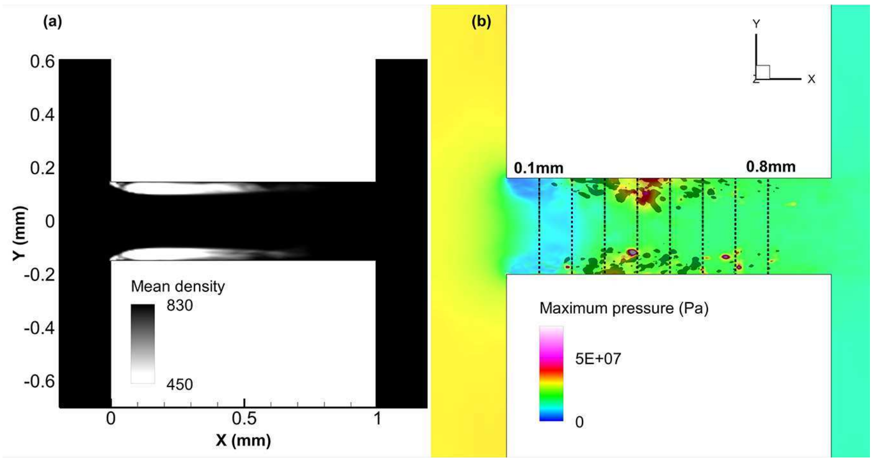

Figure 7. Indicative results from the throttle simulation: (a) the averaged density distribution and (b) pressure peak location. The black isosurface corresponds to peaks of magnitude higher than 500bar. The dashed lines are placed every 0.1mm.

As can be seen, pressure peaks are mainly located at the +y and -y walls of the throttle and not at the -z and +z. Moreover, pressure peaks start to occur after 0.1mm and almost disappear after 0.7mm, with the vast majority occurring between 0.2 and 0.6mm. Of course, the coverage of the walls with pressure peaks is rather low, but this is reasonable given the simulation time. In any case, the locations of pressure peaks is in a good agreement with the reported results.

4.3. Diesel injector - Case set-up

The Diesel injector tip geometries are shown in Figure 1. Since both injectors have five orifices, only 1/5th of the domain was considered and periodic boundary conditions have been employed at the sides of the domain. In fact, for a proper replication of the turbulence phenomena one might have to simulate the full 360^{o} of the Diesel injector, however this would impose a much higher computational cost, considering also the mesh resolution that had to be used, thus a compromise had to be made. The needle motion is assumed to be in the axial direction only, so any eccentricity effects were omitted. Eccentricity effects might be important, especially during the early opening and late closing phases, however such data are not currently available; besides including eccentricity would impose a full injector tip simulation, which, as mentioned before, would be much more computationally expensive.

Pressure boundary conditions are set according to the upstream pressure profile (Figure 2) and downstream pressure, while needle motion is set according to the lift profile. Note also that at the end of the orifice of the injector an additional hemispherical volume was added (Figure 8a), in order to move the influence of the outlet boundary further away from the orifice, especially considering that cavitation structures may reach or even exit the orifice, as it will be shown later. The configuration resembles the injection test benches (see section 2.1) where fuel is squirted into a collector filled with liquid. The computational domain was split in a set of moving, deforming and stationary zones, as shown in Figure 8a.

The computational mesh used is mainly hexahedral block-structured, with the exception of a zone in the sac before the orifice entrance, which is unstructured tetrahedral. Mesh motion is performed with a smoothing algorithm which stretches the cells in a uniform way at low lifts (from 5-40μm), while at higher lifts (40μm till max. lift) a layering algorithm has been employed, adding/removing a layer of cells as the needle moves every 7.5μm. The mesh resolution used in critical areas where cavitation develops, such as the sac volume and the orifice, is 7.5μm with additional refinement near walls. Given an average Reynolds number inside the injector orifice of ~30000, an estimation of the Taylor length scale, λ_g, is ~7μm, using the orifice diameter as a characteristic length scale, see Table I.

The needle lift was initially set at 5μm with 10 cells in the gap between needle and needle seat. Zero needle lift cannot be modelled with the methodology described so far, since this would require to change the topology of the computational mesh. Alternatively, a 'closed valve' could have been implemented with an artificial blockage at an interior boundary at the needle passage. In any case, lower lifts have been avoided, in order to prevent as much as possible high aspect ratio cells and mesh distortion, that could potentially have an impact on stability and accuracy of the results. An initial flow field was obtained from a steady state run of pure liquid flow with a laminar flow assumption. Given the fact that the Reynolds number at the minimum lift condition is ~1000, calculated using the needle lift as a length scale, not significant turbulence is expected to be generated at this stage. As will be shown later, during the opening of the needle significant turbulence develops inside the sac volume and orifice. The total cell count of the computational mesh is initially ~1million cells, but as the needle moves, additional cell layers are introduced, so the mesh size increases to ~1.75 million cells.

A bounded central scheme (hybrid between central and second order upwind) was used for momentum discretization, while second order upwind for density and QUICK for volume fraction. Time advancement was performed with an implicit, second order, backward differentiation with a time step of 5ns, in order to be able to capture the complicated turbulent patterns; the estimated CFL for this time step and the minimum cell size is ~0.5, assuming a velocity of 500m/s. The implicit time integration avoids time step restrictions due to compressibility effects, which would further limit the time step to even lower values.

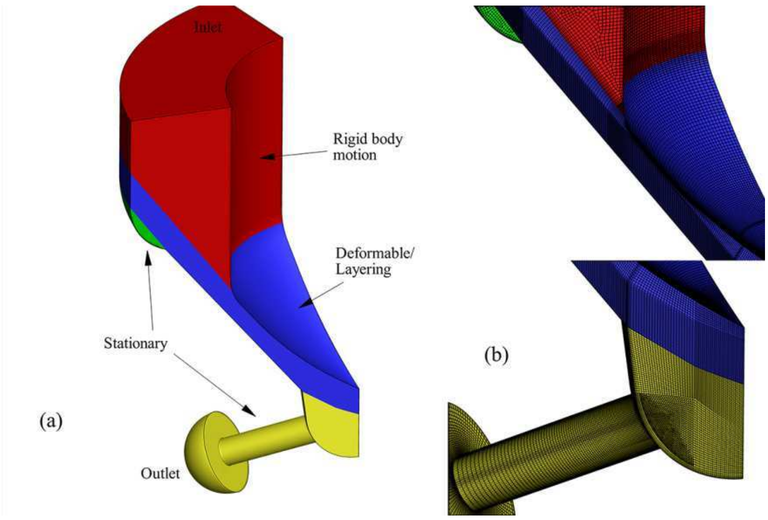

Figure 8. (a) Splitting of the geometry to accommodate mesh motion (b) details of the mesh at the needle seat passage and sac volume.

4.4. Diesel injector - simulation results

In both injectors, cavitation is predicted to occur initially at the gap between the needle and the needle seat. For design A, indicative flow field results are shown in Figure 9. At the very early opening stages of Design A injector a large part of the sac volume is filled with vapor/liquid mixture; this seems to be related to the large sac volume of the injector in combination with the needle motion profile imposed. This vaporous structure quickly collapses, causing a pressure peak at the sac wall on the axis of symmetry see also Figure 12, as flow moves in from upstream the injector and the orifice exit. Cavitation in the passage between the needle and the needle seat remains till 180μs from the beginning of the simulation, that corresponds to a needle lift of ~48μm. Cavitation inside the sac volume is caused by strong turbulence and vortices; indeed, as visible at 120μs, even at a lift of 28μm the shear layer instabilities between the liquid jet from the needle/needle seat passage and the liquid cause a very complicated flow field inside the sac volume. Note also that the liquid jet formed at the needle/needle seat passage is attached at the needle surface. Cavitation in the sac volume persists till 220μs or a lift of 65μm; beyond this point the minimum pressure in the sac volume has risen to a level of 40bar, preventing formation of cavitation. At 110μs cavitation forms at the entrance of the orifice, close to the lower orifice surface. From that point onwards, cavitation structures may span in the whole orifice length and may even exit the orifice, see also Figure 10 showing the instances of flow regions with pressure below saturation. Later on, from 280μs till 320μs there is a transition in the cavitation formation from the lower orifice surface to the upper orifice surface; as shown in Figure 9, at 320μs, corresponding to a lift of 112μm, cavitation spans on the upper orifice surface mainly. This effect coincides with the attachment of the liquid stream, moving in from upstream the injector tip, to the sac walls instead of the needle (see also Figure 9, at 320μs). From that point till the maximum lift, cavitation forms at the upper orifice surface, with occasional cavitating vortices located at the centre of the orifice.

In Figure 11 indicators of the significant turbulence in the orifice and sac volume are shown, which justify the existence of cavitating vortices. Figure 11a shows the tangential velocity distribution at four locations inside the orifice; as shown, tangential velocities may exceed 160m/s locally and may even peak at 300m/s near the orifice entrance. Figure 11b shows the coherent vortical structures that form in the sac volume, orifice and even extend beyond the injector; note that vortical strings may form inside the sac volume and extend in the orifice as well. The second invariant of the velocity gradient tensor has been used to indicate vortical structures [29], since positive values correspond to coherent vortices (also known as Q-criterion) [30, 31].

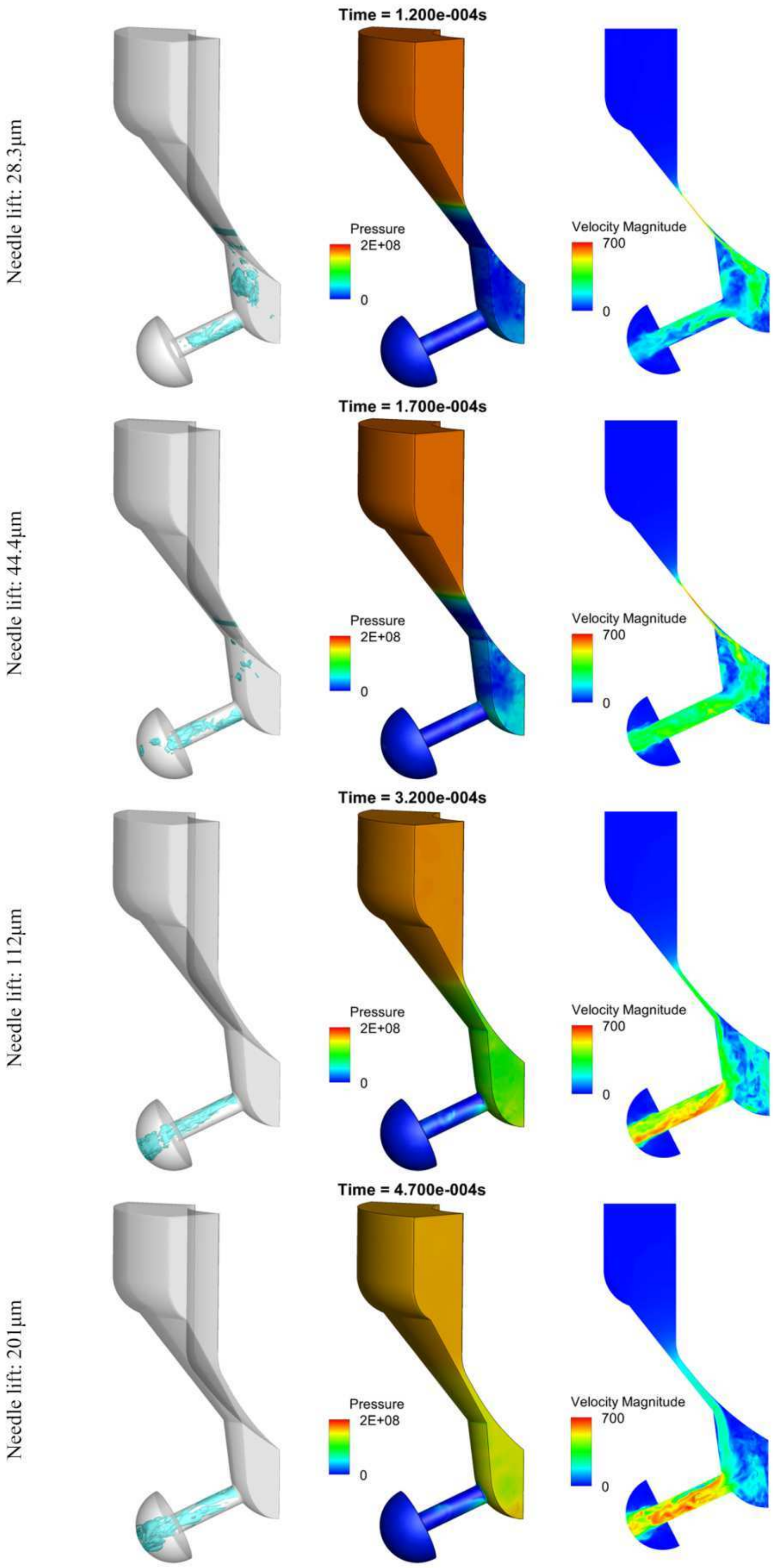

Figure 9. Indicative instances during the needle opening phase of Design A. From left to right, vapour isosurface at 50%, instantaneous pressure field and instantaneous velocity magnitude at the mid-plane of the injector.

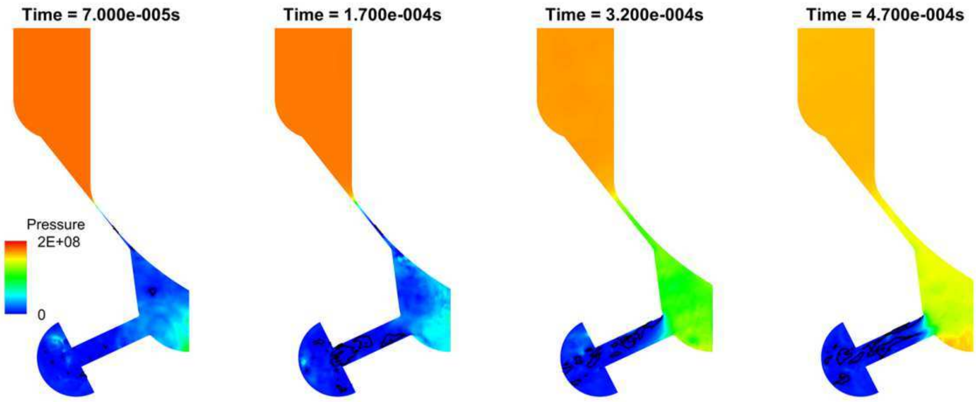

Figure 10. Instantaneous pressure field at the mid-plane of the Design A injector. The thick black line shows regions where local pressure is less or equal to saturation pressure.

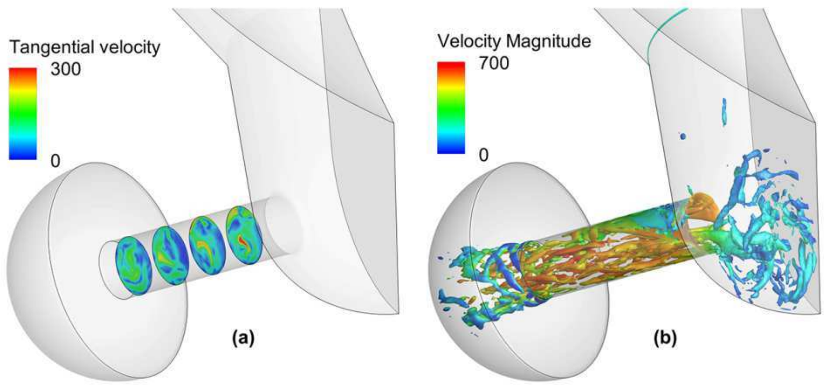

Figure 11. Design A at 560μs and 250μm lift (a) Instantaneous tangential velocity distribution on slices normal to the orifice. (b) Instantaneous isosurface of the second invariant of the velocity gradient tensor, showing vortex cores (value $5 \cdot 10^{12}$ s^{-2}) and coloured according to the local velocity magnitude.

In Figure 12 the temporal evolution of the maximum accumulated pressure peaks (that is local pressure maximum) on various injector surfaces of Design A is shown; note that red colour corresponds to peak pressures of 3000bar, purple to 3500bar and white to 4000bar. As a comparison it is mentioned that the yield stress of Stainless Steel 316 is 200-400 MPa, see [32, 33] ; thus locations of pressure peaks beyond 3000bar could indicate sites of plastic deformation/work hardening which is a prior stage of material removal. At 70μs, there is a pressure peak at the sac wall intersection with the axis of symmetry; this was observed to be caused from the initial vapour formation in the sac volume.

During the cavitation formation at the lower orifice surface (110-320μs), several pressure peaks with magnitude higher or equal to 3000bar are accumulated at the lower surface (with some peaking at 4500bar), due to vapour structure collapse; these peaks are formed from ~20% of the orifice length, downstream the entrance, till the exit of the orifice. Later on, as cavitation moves near the upper orifice surface, some scattered pressure peaks occur at the sides of the orifice. Eventually, as cavitation established at the upper orifice surface, vapour structure collapses form a cluster of pressure peaks there, almost at 45% of the orifice length, downstream the entrance. Note that the needle is free of significant pressure peaks, as well as the sac volume surface.

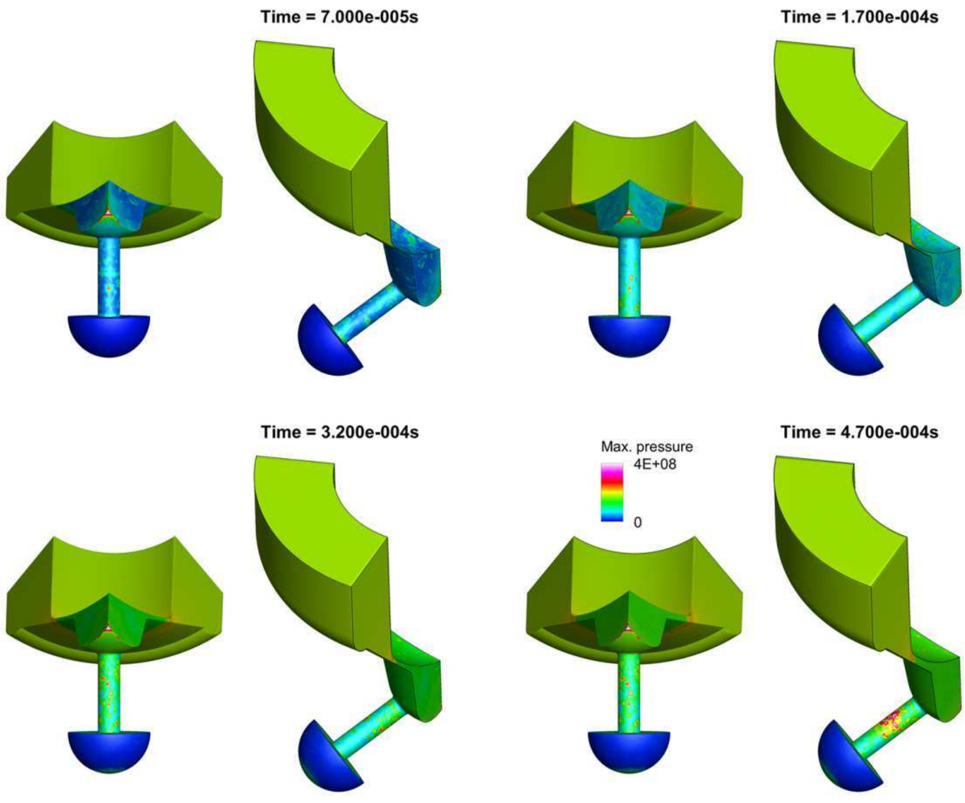

Figure 12. Time evolution of the maximum pressure on various locations of Design A injector walls.

Cavitation occurrence in Design B shows some similarities to the Design A, however there are some fundamental differences, see also Figure 14. First of all, a significant difference is that there is no vapor filling of Design B sac volume at the early opening stages. Cavitation between the needle and needle seat starts from the beginning of the injection opening till 170μs or needle lift of 74μm; comparing with Design A cavitation persists in this location at a higher lift but shorter duration (for Design A 180μs and 47μm lift). As in Design A, the jet formed at the passage, initially attaches on the needle surface, forming a large cavitating vortex inside the sac; sac cavitation first appears at 20μs or needle lift of 9μm and remains till 160μs or 67μm, which is a similar lift as Design A. The vortex formed in the sac forces the flow to enter from the lower orifice surface, beginning from 30μs and 12μm lift till 140μs and 56μm lift; cavitation at the lower orifice surface forms much earlier in Design B injector than Design A. Later, at ~160μs and 67μm lift (see Figure 14), a transition occurs that the flow attaches on the sac wall instead; from that point onwards cavitation develops at the upper orifice surface. Again, sporadic occurrence of vortex cavitation near the centre of the orifice is found, but in less extent than Design A; this is justified by the hole tapering and the developed turbulence inside the orifice, as will be shown later. As in Design A, cavitation structures may temporarily reach the orifice exit and even extend outside of the injector, see also Figure 13.

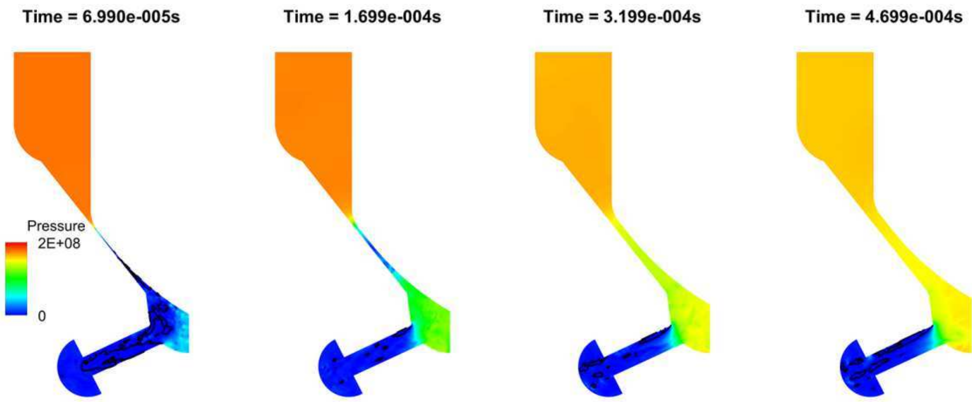

Figure 13. Instantaneous pressure field at the mid-plane of the Design B injector. The thick black line shows regions where local pressure is below or equal to saturation pressure.

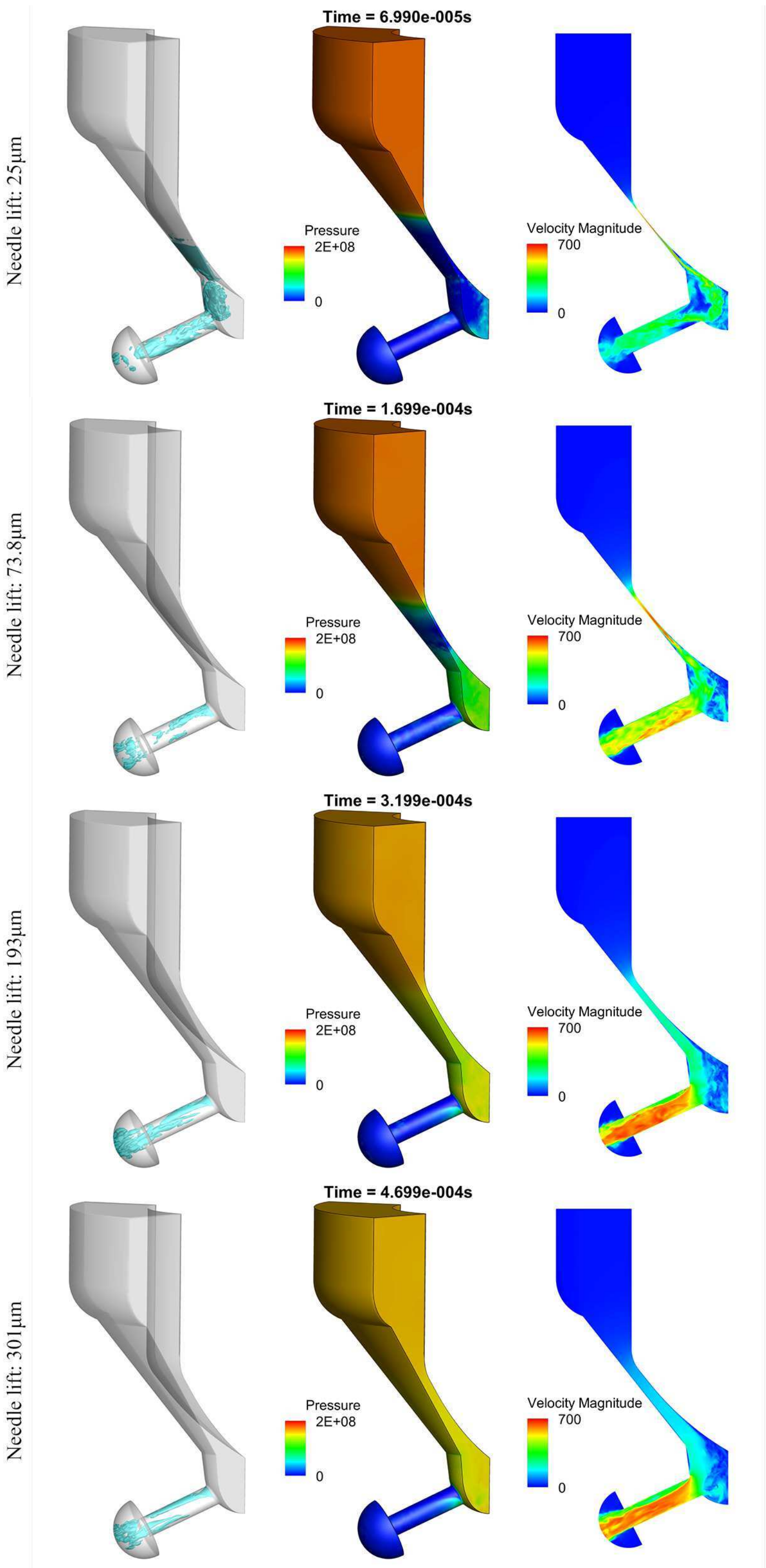

Figure 14. Indicative instances during the needle opening phase of Design B. From left to right, vapour isosurface at 50%, instantaneous pressure field and instantaneous velocity magnitude at the mid-plane of the injector.

In Figure 15a the tangential velocity distribution at four locations inside the orifice is shown, at the same lift as Design A in Figure 11a; while the maximum tangential velocity in both cases is ~300m/s and is located near the orifice entrance, the average tangential velocity in Design B is lower than the one in Design A by almost 25-45%, depending on the location; less near the orifice entrance, more near the orifice exit. In Figure 15 the coherent vortical structures are shown as an isosurface, for the same value as Design A. One observation is that vortical structures are not that developed/extended inside the orifice; this agrees with the fact that there are lower tangential velocities in the orifice slices in Figure 15a. On the other hand, there are more scattered structures throughout the whole sac volume in Design B.

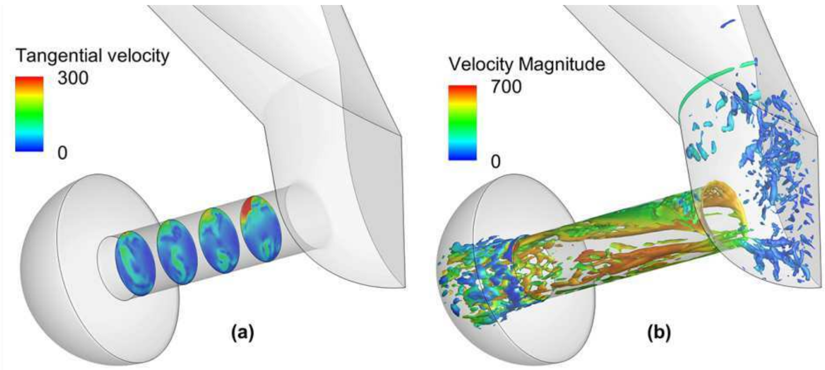

Figure 15. Design B at 400μs and 250μm lift (a) Instantaneous tangential velocity distribution on slices normal to the orifice. (b) Instantaneous isosurface of the second invariant of the velocity gradient tensor, showing vortex cores (value $5 \cdot 10^{12}\ s^{-2}$) and coloured according to the local velocity magnitude.

In Figure 16 the temporal evolution of the maximum accumulated pressure peaks on various injector surfaces of Design B are shown. Here it is visible that very early, at 70μs, the intense cavitation in the sac volume causes significant pressure peaks at the needle surface; actually wall pressure peaks may even reach instantaneous values of over 5000bar (local pressure at spots of the bulk liquid volume may locally reach 9000bar). Later on, after 320μs, pressure peaks start to form at the upper orifice surface, due to cavity shedding developing near this region. Also, some spots of pressure peaks appear on the sac volume, whereas the lower orifice surface is totally clean of pressure peaks.

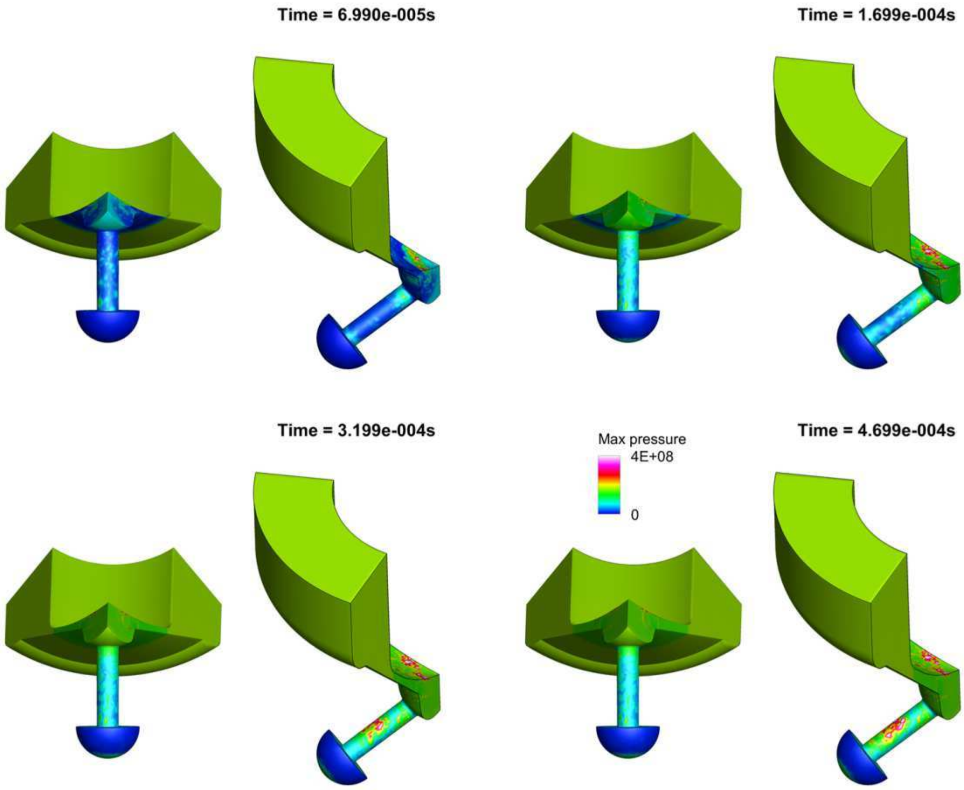

Figure 16. Time evolution of the maximum pressure on various locations of Design B injector walls.

5. Discussion

Cavitation presence in the sac volume of the Design B was found to be higher than that of Design A injector, without considering the initial vapour filling of Design A (which is probably due to the imposed needle motion at the first time steps). Whereas there is no significant difference in the velocity field development in the two injectors, i.e. the flow initially attaches on the needle and then on the sac, the fundamental difference is that in Design B the needle moves faster than in Design A, by ~50%. At low lifts, this reduces the pressure in Design B sac causing more cavitation there, due to the imposed flow acceleration from the fast needle displacement.

On the other hand, cavitation presence in the form of cavitating vortices is more extensively found in the orifice of Design A injector; the same applies for flow turbulence. This seems to be related to the hole tapering; indeed the cylindrical hole of Design A injector promotes cavitation formation. On the other hand, the conical orifice in Design B injector reduces the amount of cavitation vortices inside the hole, leaving almost only a vaporous layer at the upper orifice surface. The flow is also more ordered and with less tangential velocity component in the orifice sections of Design B injector. Another way to illustrate these effects is by examining the mass flow rate and the average vapour fraction at the orifice exit, as shown in Figure 17: the liquid fraction and the mass flow rate is higher in Design B injector at high lifts operation. Note also that at the early opening stages of Design A injector a slight flow reversal is found at the injector outlet; as before, this is related to the imposed needle motion and the significantly large sac volume of Design A.

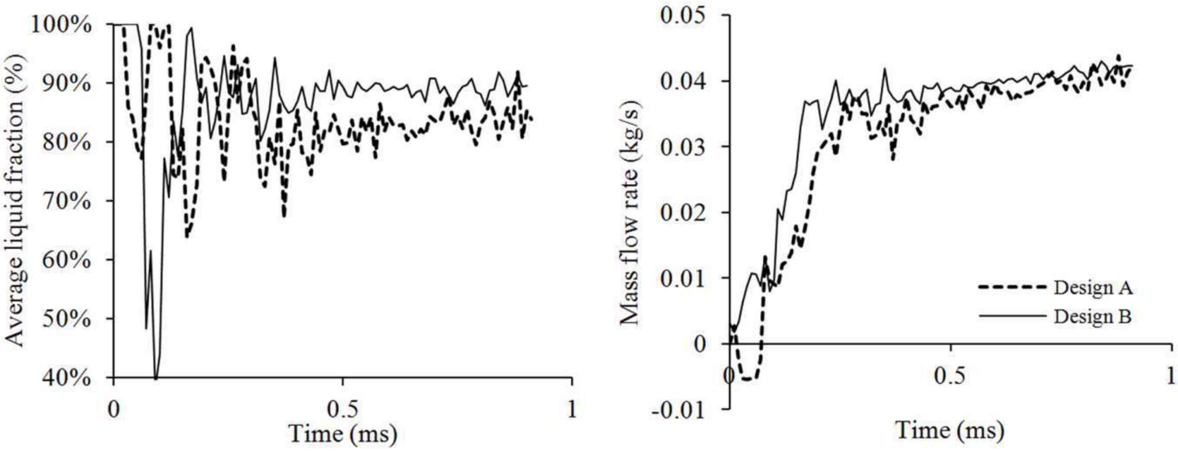

Figure 17. Average liquid volume fraction and mass flow rate through the orifice exit for the examined injectors - opening phase. The jagged lines are due to the low sampling rate.

An important observation for the flow in both injectors is that, even though the flow is well ordered upstream the injector and in the passage between the needle and the needle seat, there is significant turbulence generation inside the sac volume, due to the sudden expansion, and the orifice, due to the strong flow direction change. Indeed, the maximum Reynolds number at the annulus upstream the tip is ~10000, occurring at the maximum lift; this means that the flow upstream the injector tip will be transitional at maximum lift and laminar at lower lifts. Information on possible turbulent fluctuations upstream the injector tip have not been prescribed, since currently such data are not available. Still, the presence of significant turbulence downstream the needle/needle seat passage can be explained by the strong shear instabilities of the fuel stream rushing in the sac volume.

Regarding erosion prediction for Design A injector, pressure peaks significantly exceeding 3000bar are found at scattered spots at the lower orifice surface, spanning from 20% of the orifice length till the exit of the orifice, and a densely populated pressure peak region at the upper orifice surface, see Figure 18. Both of these facts could potentially correlate to the erosion patterns of Design A in some cases, e.g. see Figure 4. Such pressure values are comparable to the yield stress of metal alloys, thus the existence of such collapses can detrimentally contribute to local fatigue. Material exposed at such pressures, over time may undergo plastic deformation and material removal, changing the local flow field and potentially enhancing cavitation damage downstream. Simulations indicate that the needle of Design A injector is practically clear of high pressure peaks, which also correlates well with the barely observable erosion from the experiments.

A good trend is found for Design B as well; from the experiments a clear pattern is identified with erosion formation on the needle surface in the form of a deeply engraved ring shape, at the upper orifice surface and at some spots on the sac wall upstream the orifice. As shown in Figure 19, these locations are predicted very well from the simulations:

- High pressure peaks are found in a circular pattern on the needle of Design B injector. Local pressures may exceed 5000bar.

- Pressure peaks of more than 4000bar are found at the upper orifice hole in a clustered arrangement. The lower orifice surface is clean of high pressure peaks.

- Sporadic pressure peaks of pressures higher than 3500bar are found at the sac wall.

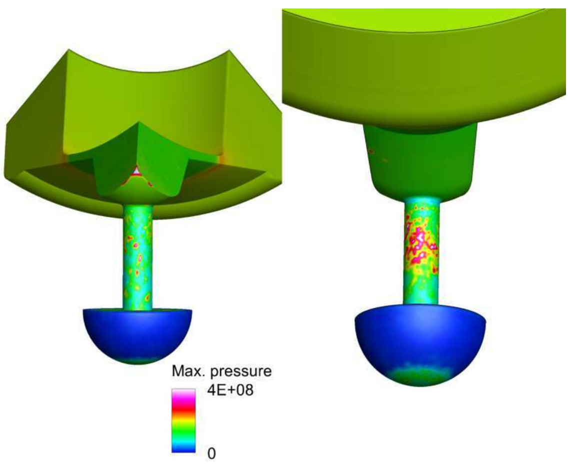

Figure 18. Accumulated pressure peak distribution at various locations of Design A.

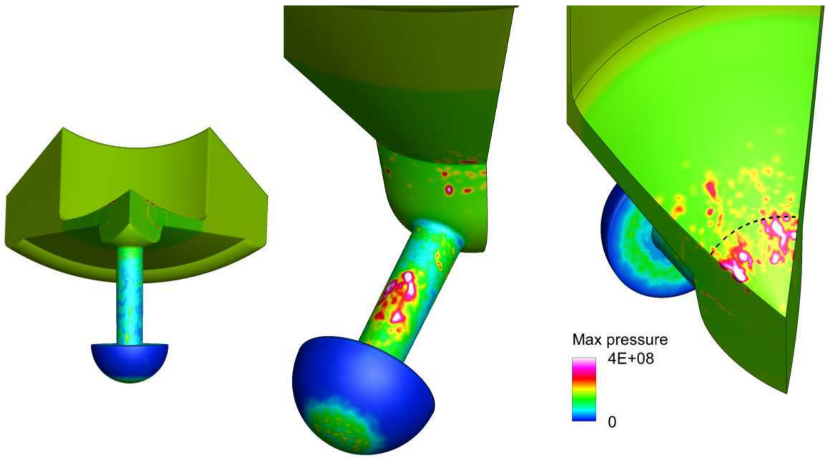

Figure 19. Accumulated pressure peak distribution at various locations of the Design B. The dashed line denotes a radius of 0.6mm.

Unfortunately, the simulation is very demanding from a computational point of view, requiring significant time to compute, mainly due to the very small time step required. These simulations have been running each on one 12CPU Xeon E5-2630 v2 @ 2.6GHz computer for 3 months to get to this point; potentially there could be a benefit by running in a distributed parallel environment with much more processors.

6. Conclusion

This paper outlines the potential of 2-phase cavitation models in the prediction of erosion effects, by tracking the Rayleigh collapse of vapor structures. The methodology is tested in a benchmark case of the collapse of a spherical vapor bubble. Then, it is applied in a more complicated case of a throttle resembling the injector passages and the opening phase of a Diesel injector. LES turbulence models have been used, since in the cavitation literature there are enough indications that RANS/URANS models may be situational. Erosion in complicated geometries is correlated to pressure peaks that form during the collapse of vapor structures. In the injectors examined, these peaks may reach pressures of more than 4000bar, depending on the location. It is highlighted that such pressures are higher than the yield stress of common materials, e.g. SS316, and can contribute to the plastic deformation of material which is the first stage in the work hardening process before material removal. Indicative CT scans are provided for the two examined injectors after endurance testing. CFD results of Design A show some resemblance to the experimentally observed erosion patterns; the needle is free of erosion, whereas pressure peaks are found inside the orifice, at both upper and lower surfaces. Design B shows a much greater consistency in the erosion development. Moreover there is very good agreement of the predicted pressure peak locations with the observed erosion patterns: high pressure peaks are found on the needle surface, at the upper orifice surface and at sporadic locations of the sac wall, all being in accordance with the experiment. The present work's novelty is to use such a methodology in a diesel injector with a moving needle and correlating the pressure peaks due to vapor collapse with erosion damage, determined from experiments. Continuation of this work will involve examination of further injection stages, as well as possible inclusion of eccentricity effects or upstream turbulence fluctuations, should these information be available.

Disclaimer

Nomenclature

D_{in}	Orifice entrance diameter (m)
D_{out}	Orifice exit diameter (m)
p	Pressure (Pa)
B	Bulk modulus (Pa)
ρ	Density (kg/m^3)
$\rho_{sat,L}$	Density at saturation (kg/m^3)
n	Tait equation exponent (for liquid) (-)
p_{sat}, p_v	Saturation/Vapour pressure (Pa)

μ_L	Dynamic viscosity of the liquid (Pa·s)
a	Vapour fraction (-)
ρ_v	Vapour density
$\mathbf{u}$	Velocity field
R_e	Evaporation rate (kg/m^3/s)
R_c	Condensation rate (kg/m^3/s)
μ_V	Vapour dynamic viscosity (Pa.s)
R	Bubble radius (m), index 0 denotes initial radius
p_∞	Pressure at far field (Pa)
τ	Rayleigh time (s)
λ_g	Taylor length scale (m)

Acknowledgements

The research leading to these results has received funding from the People Programme (IAPP Marie Curie Actions) of the European Union's Seventh Framework Programme FP7/2007-2013/ under REA grant agreement n. 324313.

References

[1] Sezal I. *Compressible Dynamics of Cavitating 3-D Multi-Phase Flows*, in *Fakultat fur Maschinenwesen*2009, Technischen Universitaet Muenchen.

[2] Sezal IH, Schmidt SJ, Schnerr GH, Thalhamer M, and Förster M. Shock and wave dynamics in cavitating compressible liquid flows in injection nozzles. *Shock Waves* 2009; **19**(1): p. 49-58 DOI: 10.1007/s00193-008-0185-3.

[3] Salvador FJ, Romero JV, Roselló MD, and Martínez-López J. Validation of a code for modeling cavitation phenomena in Diesel injector nozzles. *Mathematical and Computer Modelling* 2010; **52**(7–8): p. 1123-1132 DOI: http://dx.doi.org/10.1016/j.mcm.2010.02.027.

[4] Salvador FJ, Carreres M, Jaramillo D, and Martínez-López J. Analysis of the combined effect of hydrogrinding process and inclination angle on hydraulic performance of diesel injection nozzles. *Energy Conversion and Management* 2015; **105**: p. 1352-1365 DOI: http://dx.doi.org/10.1016/j.enconman.2015.08.035.

[5] Salvador FJ, Martínez-López J, Caballer M, and De Alfonso C. Study of the influence of the needle lift on the internal flow and cavitation phenomenon in diesel injector nozzles by CFD using RANS methods. *Energy Conversion and Management* 2013; **66**: p. 246-256 DOI: http://dx.doi.org/10.1016/j.enconman.2012.10.011.

[6] Molina S, Salvador FJ, Carreres M, and Jaramillo D. A computational investigation on the influence of the use of elliptical orifices on the inner nozzle flow and cavitation development in diesel injector nozzles. *Energy Conversion and Management* 2014; **79**: p. 114-127 DOI: http://dx.doi.org/10.1016/j.enconman.2013.12.015.

[7] Salvador FJ, Martínez-López J, Romero JV, and Roselló MD. Computational study of the cavitation phenomenon and its interaction with the turbulence developed in diesel injector nozzles by Large Eddy Simulation (LES). *Mathematical and Computer Modelling* 2013; **57**(7–8): p. 1656-1662 DOI: http://dx.doi.org/10.1016/j.mcm.2011.10.050.

[8] Örley F, Hickel S, Schmidt SJ, and Adams NA. LES of cavitating flow inside a Diesel injector including dynamic needle movement. *Journal of Physics: Conference Series* 2015; **656**(012097) DOI: 10.1088/1742-6596/656/1/012097.

[9] Patouna S. *A CFD study of cavitation in real size Diesel injectors* in *Departamento de Maquinas y Motores Termicos* 2012, Universitat Politecnica de Valencia: Valencia.

[10] Strotos G, Koukouvinis P, Theodorakakos A, Gavaises M, and Bergeles G. Transient heating effects in high pressure Diesel injector nozzles. *International Journal of Heat and Fluid Flow* 2015; **51**(0): p. 257-267 DOI: http://dx.doi.org/10.1016/j.ijheatfluidflow.2014.10.010.

[11] Devassy M, Caika V, Sampl P, Edelbauer W, and Greif D. Numerical investigation of cavitation injector flow accounting for 3D-needle movement and liqid compressibility effects. in *Fuel Systems for IC Engines*, IMechE, London 2014.

[12] Gavaises M, Papoulias D, Andriotis A, Giannadakis E, and Theodorakakos A. Link Between Cavitation Development and Erosion Damage in Diesel Injector Nozzles. *SAE Technical Paper 2007-01-0246* 2007 DOI: 10.4271/2007-01-0246.

[13] Koukouvinis P, Bergeles G, Li J, Wang L, Theodorakakos A, and Gavaises M. Simulation of cavitation inside diesel injectors, including erosion modelling. in *Fuel Systems for IC Engines*, IMechE, London 2014.

[14] Kolev N. *Multiphase Flow Dynamics 3*. 2007: Springer Berlin Heidelberg.

[15] Coutier-Delgosha O, Reboud JL, and Delannoy Y. Numerical simulation of the unsteady behaviour of cavitating flows. *International Journal for Numerical Methods in Fluids* 2003; **42**: p. 527-548 DOI: 10.1002/fld.530.

[16] Edelbauer W, Strucl J, and Morozov A. Large Eddy Simulation of cavitating throttle flow. in *SimHydro 2014:Modelling of rapid transitory flows*, Sophia Antipolis 2014.

[17] Egler W, Giersch JR, Boecking F, Hammer J, Hlousek J, Mattes P, Projahn U, Urner W, and Janetzky B, *Fuel Injection Systems*, in *Handbook of Diesel Engines*, Mollenhauer K and Tschöke H, Editors. 2010, Springer-Verlag Berlin Heidelberg. p. 127-174.

[18] ANSYS. *ANSYS Fluent 15.07*, 2013.

[19] Lemmon EW, Huber ML, and McLinden MO. *NIST Standard Reference Database 23: Reference Fluid Thermodynamic and Transport Properties-REFPROP, Version 9.1*, 2013, National Institute of Standards and Technology, Standard Reference Data Program: Gaithersburg.

[20] Ivings MJ, Causon DM, and Toro EF. On Riemann solvers for compressible liquids. *International Numerical Methods for Fluids* 1998; **28**: p. 395-418 DOI: 10.1002/(SICI)1097-0363(19980915)28:3<395::AID-FLD718>3.0.CO;2-S.

[21] Ji B, Luo X, Wu Y, Peng X, and Duan Y. Numerical analysis of unsteady cavitating turbulent flow and shedding horse-shoe vortex structure around a twisted hydrofoil. *International Journal of Multiphase Flow* 2013; **51**(0): p. 33-43 DOI: http://dx.doi.org/10.1016/j.ijmultiphaseflow.2012.11.008.

[22] Franc J-P and Michel J-M. *Fundamentals of Cavitation*. 2005: Kluwer Academic Publishers.

[23] Brennen C. *Cavitation and Bubble Dynamics*. 1995: Oxford University Press.

[24] Trevena DH. Cavitation and the generation of tension in liquids: Review article. *Journal of Physics D: Applied Physics* 1984; **17**: p. 2139-2164 DOI: 10.1088/0022-3727/17/11/003.

[25] Heyes DM. Liquids at positive and negative pressure. *Physica Status Solidi (B)* 2008; **245**(3): p. 530-538 DOI: 10.1002/pssb.200777706.

[26] Kobayashi H and Wu X. *Application of a local subgrid model based on coherent structures to complex geometries*, 2006, Center for Turbulence Research. p. 69-77.

[27] Nicoud F and Ducros F. Subgrid-scale stress modelling based on the square of the velocity gradient tensor. *Flow, Turbulence and Combustion* 1999; **62**: p. 183-200.

[28] Pope S. *Turbulent Flows*. 2000: Cambridge University Press.

[29] X. Jiang and Lai CH. *Numerical techniques for direct and large eddy simulations*. Numerical analysis and scientific computing. 2009: Chapman & Hall / CRC. 276

[30] Green MA, Rowley CW, and Haller G. Detection of Lagrangian Coherent Structures in 3D Turbulence. *Journal of Fluid Mechanics* 2007; **572**: p. 111-120.

[31] Wu JZ, Ma HY, and Zhou MD. *Vorticity and Vortex Dynamics* 1ed. 2006: Springer-Verlag Berlin Heidelberg.

[32] Young SG. *Cavitation damage of stainless steel, nickel and an aluminum allow in water for ASTM round robin tests*, 1968, National Aeronautics and Space Association: Washington D.C.

[33] Berchiche N, Franc JP, and Michel JM. A Cavitation Erosion Model for Ductile Materials. *ASME Journal of Fluids Engineering* 2002; **124**: p. 201-207 DOI: 10.1115/1.1486474.